Purdue University
School of Civil Engineering
Geotechnical Engineering

CE-597

Non-linear fracture mechanics

Term Project

Numerical Simulation of Crack Propagation in Rocks under Uniaxial Compression

Professor: Pablo Zavattieri
Students: Felipe Ochoa
Ahmadreza Hedayat
Yazen Khasawneh
Due Date: 04/29/2011

Table of Content

1 Introduction

1.1 Motivation

Deformation and fracture are complex processes, presenting interactions between different phases in a material subjected to loading. These interactions can have micro and macro components, being prone to develop crack initiation and, likely propagate throughout a body.

The current project report is on numerical simulation of brittle behavior under mixed mode failure (mode 1 and 2 combined) for rocks, to study the fracture process in a homogeneous experimental sample of rock called gypsum , which has a flaw within it, having different sizes and orientations respect to the horizontal. To perform the numerical simulations, the finite element program ABAQUS and the boundary element method program FROCK will be used, taking into account different stages in the entire process of fracture: Since the crack growth starts at the opening of the existing flaw in the material, up to the propagation throughout the body, and its subsequent growth. It is analyzed how this initial flaw initiates the formation of macrocracks, and eventually gets the body to a state of complete failure.

It is necessary to remark that appropriate continuum mechanical failure models are difficult to solve without advanced tools, being the use of advanced techniques required to describe the failure mechanism of some loading condition. For such problems, numerical methods have been developed to simulate failure mechanisms in materials, being the Finite Element Method (FEM) a method that provides a reasonable way to predict the failure behavior of materials, optimizing the microstructure of brittle materials behavior. However, in the case of fracture mechanics, provided the inherent complex nature related to the separation of elements in the processes of crack initiation and crack growth, a different technique to simulate them is required. For this, cohesive laws implemented in finite elements are necessary to do these studies. The basis for cohesive zone models can be traced back to the works of Dugdale in 1960 and Barenblatt in 1962. The implementation of these cohesive zone models is available for its use in ABAQUS. Also, XFEM method analysis is available in ABAQUS to perform the analysis of the fracture development.

1.2 Problem statement

Rock fracture and the mechanisms responsible of the initiation and propagation of cracks are essential for the design in rock mechanics problems. As most of the different kind of rocks found in nature have

fractures of the brittle type, the Griffith hypothesis is used to explain fracture initiation, based on the assumption that in the material small cracks or flaws, are present.

Based on this, numerical analysis results for a rock gypsum sample will be presented to explain how the fracture theory is applicable to brittle behavior of rocks, in particular, for the case of a preexisting crack in a body, and subjected to tensile stresses. The flaw has different orientations respect to the plane of loading, causing a combination of failure modes, which are shown in Figure 1.

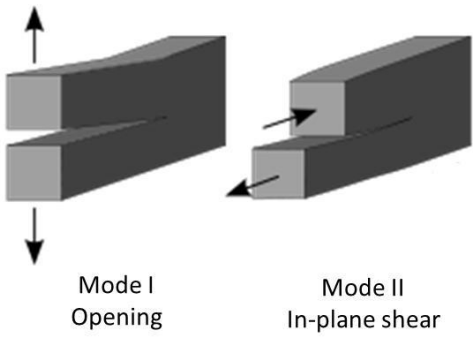

Figure 1: Mode failures combined in the analysis

The specific problem to study this combined mode of failure is shown in Figure 2.

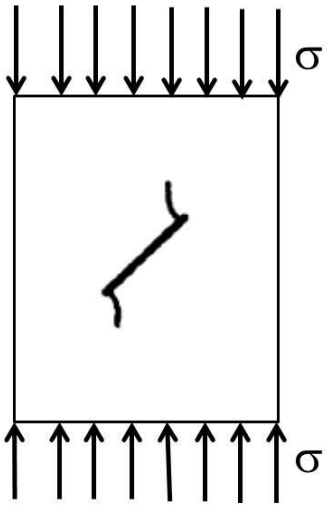

Figure 2: Crack propagation for a specimen with an oriented flaw

The process of initiation of crack and crack growth in the sample of Gypsum will be analyzed, to confirm some of the experimental observations made on rock samples presenting mixed modes of failure.

1.3 Organization

The report is organized as follows:

The second part presents a short introduction and a literature review of the problem stated, showing experimental studies of rock specimens having one single flaw, subjected to a stress state producing a mixed mode of failure. The third part presents the numerical simulation of the phenomenon of crack initiation and propagation observed in FROCK and ABAQUS. For this, a brief theoretical description of the models used–Boundary Element Method, Cohesive Models and XFEM method–along their corresponding theoretical backgrounds, mesh properties and results obtained for each case, is provided. The last part will present the results and conclusions obtained.

2 Literature review

Extensive research has been conducted to explain the initiation and propagation of cracks in rock samples, to address its behavior as a brittle material, in which mainly, two types of cracks are most common when a flaw exists in a body of rock: wing cracks and secondary cracks.

Wing cracks are tensile cracks initiating in the area close to the tip of the pre-existing flaw. They propagate in a stable manner along the direction of maximum compression, as shown in Figure 3.

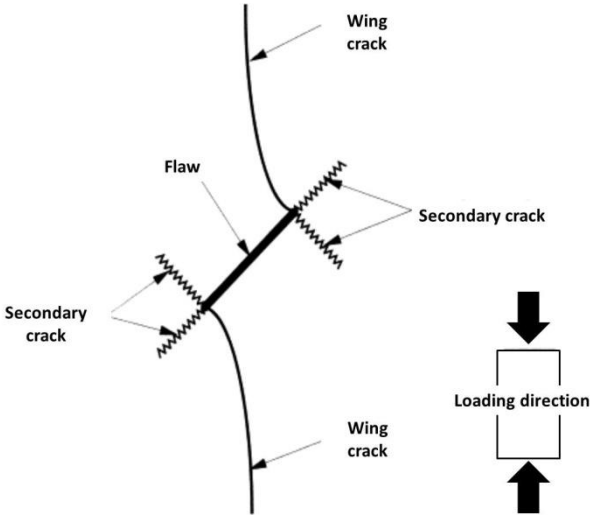

Figure 3: Initiation of tensile wing cracks at a pre-existing inclined fracture in uniaxial compression

On the other hand, secondary cracks, which can be of either shear or tensile nature, initiate after the primary cracks have developed.

2.1 Crack development in uniaxial compression

To study the development of cracks in rocks, uniaxial compression tests on Plaster of Paris specimens containing a single flaw, of different dimensions and orientations respect to the horizontal, were performed (Lajtai, 1975). The stages of the crack development (Figure 4), can be summarized as follows:

(a) Tensile fractures: First to appear. They propagate in a stable manner, following a curvilinear path, becoming parallel to the applied load.
(b) Normal shear fractures: These cracks initiate within a compressive stress area at the tip of the flaw, propagating normal to the direction of applied load.
(c) Extension of tensile and normal shear fractures: A shear zone around the crack tip, formed as the applied load increases.
(d) Expansion of the shear zone in axial direction: Inclined shear fractures are formed in the shear zone, resulting in a loss of cohesive strength in the material.

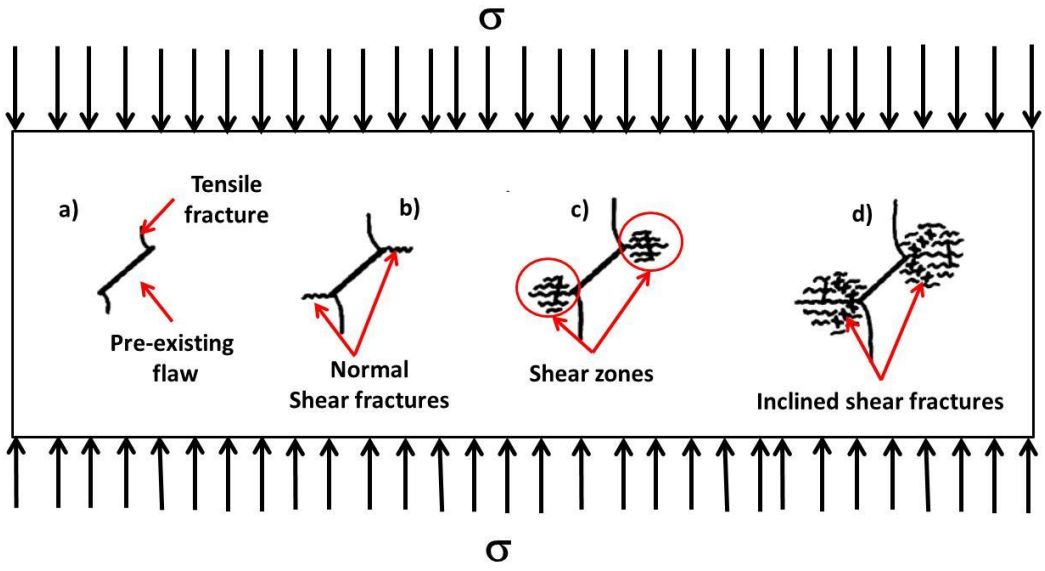

Figure 4: Fracturing pattern observed in open flaw specimens (Lajtai, 1975)

Ingraffea and Heuze (1980) performed uniaxial compression tests on different materials such as glass, acrylic, plastic polymer and rocks having a single flaw, observing that primary cracks are initiated at points with the highest tension. However, secondary cracks, which originated at points of high compressive stress, were observed to appear only in rock.

Likewise, the crack initiation and propagation of a single flaw (10 mm long and 0.2 mm wide), in a limestone sample was tested, observing secondary cracks initiating at points within a distance away from the flaw tips, naturally and schematically shown by circles in Figure 5.

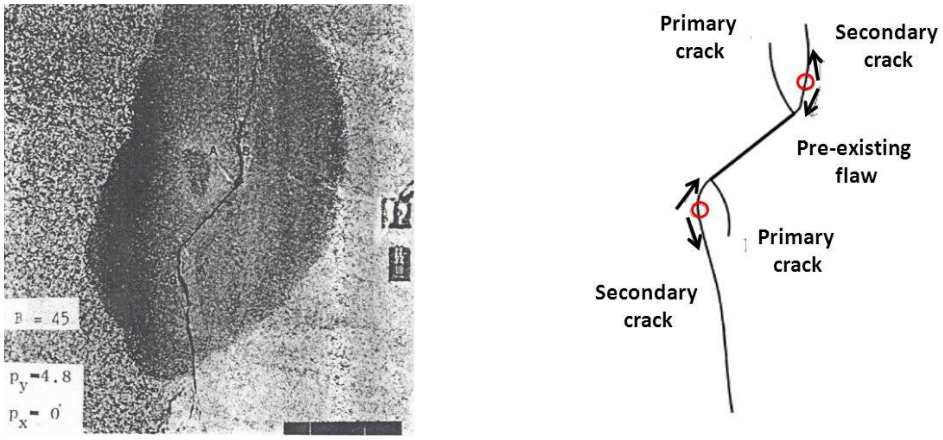

Figure 5: Primary and secondary cracks initiated from a single flaw in limestone in uniaxial compression by Ingraffea and Heuze (1980). left) real image , and (right) sketch of cracking pattern.

Other experimental tests have been performed on high and low porosity sandstones (Petit and Barquins, 1988), observing branch fractures (noted bf, instead of tensile wing cracks) initiating at stress level of about half the strength of the material tested. For the high porosity sandstone, a shear zone (sz) at the tip of the flaw was observed along its plane. In the low porosity sandstones, microcracks occurred at the tips of the flaw and produced the initiation of branch cracks, and shear cracks propagated in two different directions. Shear cracks occurred suddenly near the peak strength of the material and propagated in an unstable manner, as shown in Figure 6.

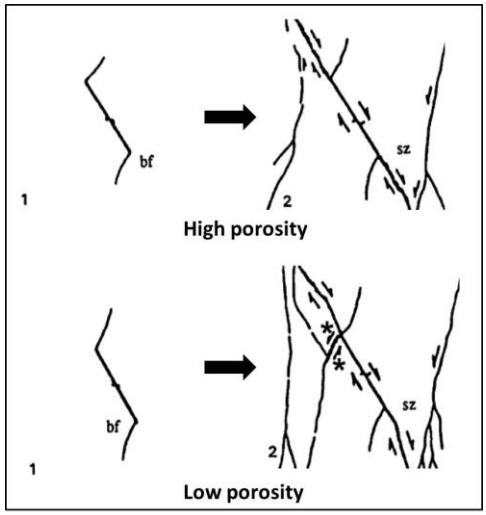

Figure 6: Crack grows from a single flaw in low and high porosity sandstone by Petit and Barquins (1988)

Uniaxial compression tests on marble plates (Huang et al, 1990) were conducted on specimens containing single flaws (20 mm long and less than 1 mm opening) revealed crack stages (Figure 7), which present the following sequences: (1) Initiation and propagation of primary forward tensile cracks (PFTCs), (2) initiation and propagation of secondary forward tensile cracks (SFTCs), (3) Initiation of shear belts (Backward shear belts (BSBs) and forward shear belts (FSBs), (4) Initiation and propagation of backward tensile cracks (BTCs), and finally (5) specimen failure.

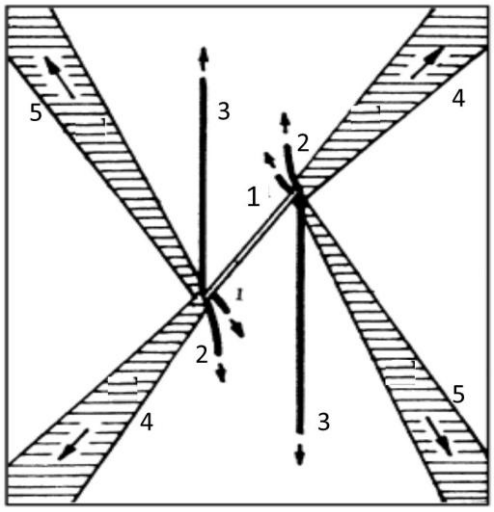

Figure 7: Cracking features in Marble specimens tested by Huang et al. (1990): 1- PFTCs: Primary Forward Tensile Cracks, 2- SFTCs: Secondary Forward Tensile Cracks, 3- BTCs: Backward Tensile Cracks, 4- FSHs: Forward Shear Belts, 5- BSBs: Backward Shear Belt

The path and kinetics of tensile wing crack propagation were studied using acrylic (PMMA) plate samples, with flaws of 0.3 mm wide and 10 mm long, oriented at different angles respect to the loading axis (Barquins and Petit, 1992). Figure 8 shows the symmetric wing tensile crack formed in biaxial compression test. As shown in Figure 8, primary and secondary cracks are clearly seen.

Figure 8: Uniaxial testing with two symmetrical wing cracks in PMMA plate after Barquins and Petit (1992)

Chen et al. (1995) observed flaw coalescence of cracks, on pre-cracked marble plates, containing 0.1 mm wide single flaws, subjected to uniaxial compression, having wing tensile cracks first occurring near the tip of the flaw, and propagating perpendicular to the direction of flaw in (Figure 9). It also was observed that secondary cracks, initiated from the tip of the flaw, propagating along the loading direction Figure 9 (c). Finally, an 'x' shaped band crack from the flaw tips induced failure in the specimen (Figure 9 (d)).

Li et al. (2005) conducted uniaxial compression tests on Huangshi marble specimens with a single crack 0.5-1 mm width. Specimens were tested in two different orientation angles, observing the following crack growth pattern: (a) single flaw with 35˚ with the horizontal- tensile wing cracks propagated from the tip of the flaw, and (b) single flaw with 45˚ with the horizontal- primary and secondary cracks initiated and propagated from the flaw tips in a stable manner (Figure 10).

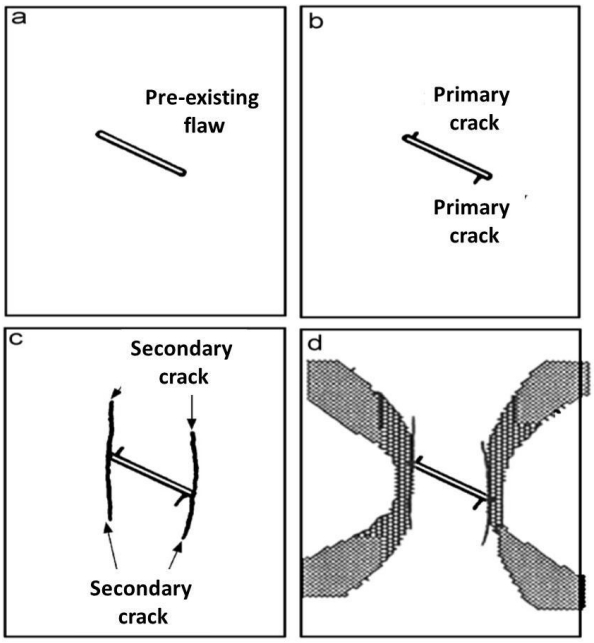

Figure 9: Various stages of crack growth from a single flaw in marble after Chen et al., (1995)

Most of the studies mentioned above show that cracks can be categorize mainly as primary and secondary, being reasonable to assume the use of the term primary cracks as the tensile wing cracks and secondary cracks as shear cracks.

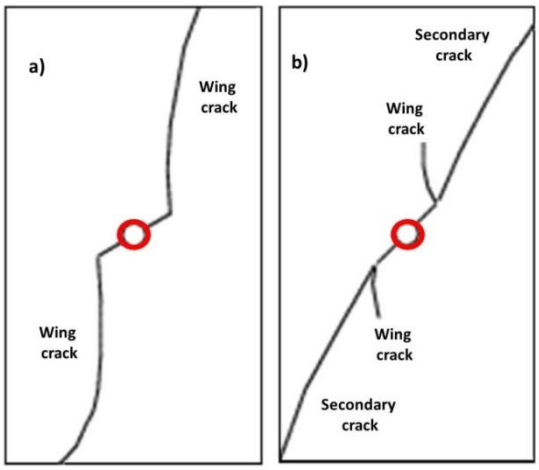

Figure 10: Crack development from a single flaw in marble after Li et al. (2005)-(a) tensile wing cracks initiated from the 35˚ flaw, (b) wing cracks and secondary cracks in a 45˚ flaw

In addition, Wong and Einstein (2009) studied the cracking behavior of molded gypsum and Carra marble specimens under uniaxial compression, on specimens having single flaws of 12.5 mm long and different orientations. The cracking process was monitored and recorded with a high speed camera, to identify the crack types. From these observations, seven crack types could be observed, with different cracking mechanism initiated at the pre-existing flaw, as a result of the applied uniaxial load (Figure 11).

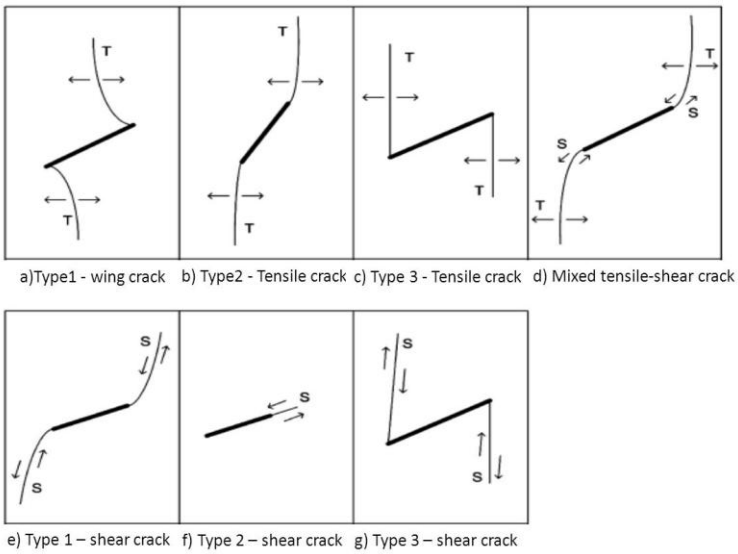

Figure 11: Crack types initiating at a single flaw in uniaxial compression (Wong & Einstein, 2009)

From these examples, it can be remarked that, in brittle rock specimens having single flaws, and subjected to uniaxial compression, it is observed that tensile cracks are initiated and propagate in a stable manner, being these tensile wing cracks the most general cracks, propagating in a curvilinear path as the load increases, aligning along the direction of maximum compressive load.

Unlike primary cracks, shear cracks never initiate the cracking process; It is the additional shear loading which induces secondary cracks. In some cases, these secondary cracks are shear cracks, while in some others, secondary forward tensile cracks were observed to happen after the primary cracks, being the failure generally caused by the generation of secondary cracks towards the boundary of the specimen.

Based on these observations, it is generally accepted that the first fractures in a brittle material loaded in uniaxial direction are of tensile nature. The opening of these cracks faces parallel to the applied load and closure of crack faced perpendicular to the applied load.

3 Numerical simulation of crack propagation

The numerical analysis of brittle damage of materials and subsequent failure is based on a micromechanical description of its failure process. Below, numerical simulations of the cracking process and its propagation in an experimental sample of gypsum is described and detailed.

The simulations will be performed with a Boundary Element Method program called FROCK, and the finite element method program called ABAQUS, working with Cohesive zone model elements and

also with XFEM tools. A brief description of the different models will be given, with their corresponding theoretical backgrounds, along with the model description, mesh properties and results obtained for each case.

The numerical problems deal with the global load-displacement response as well as the onset, size and orientation of localized damage zones and crack in the rock specimen modeled, in order to guarantee the reliability of the obtained results.

3.1 Boundary element method

3.1.1 Theoretical background

The boundary element method (BEM) is a numerical technique that has become an important alternative for the solution of a number of physical problems. In common with the better-known finite element method (FEM) and finite difference method (FDM), BEM solves partial differential equations (PDEs) and its convergence is obtained when the problem is stated in this manner.

BEM has provided flexible and efficient computer-based solutions to different engineering problems, finding successful solutions in topics such as stress analysis, potential flaw and fracture mechanics.

BEM is derived through the discrete idealization of an integral equation, which is mathematically equivalent to the original partial differential equation. The essential re-formulation of the PDE related to the problem, consists of an integral equation that is defined on the boundary of the domain of study. This equation is termed boundary integral equation (BIE), being BEM often referred to as the boundary integral equation method or boundary integral method.

The reformulation of an integral equation can only be derived for certain classes of PDE. Therefore, the BEM is not widely applicable as finite element and finite difference methods. However, when it is applicable, the method is easier to use and more efficient than usual methods.

The fact that only the boundary of the domain of the PDE requires sub-division, represents a great advantage, as the problem is reduced in one dimension, in contrast to what happens with finite difference or finite element method, in which the whole domain of the PDE requires subdivision. Hence, BEM a transforms a volume problem into one over its surface, and in two dimensions, only the boundary contour is discretized as shown in Figure 12. The integral equations related to BEM are valid everywhere inside the domain of the boundary defined for the problem.

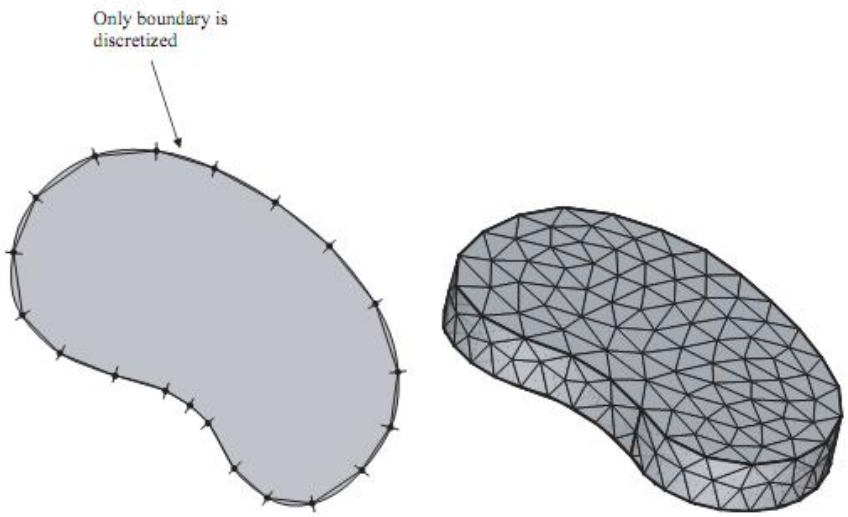

Figure 12: Volume and boundary elements in a solid

To solve the equations related to a BEM problem, an algorithm known as the Galerkin method is employed to numerically approximate the solution of boundary integral equations. To introduce the solution, consider the three-dimensional Laplace equation, $\nabla^2\varphi = 0$ defined in a 3D domain. The corresponding integral equation for the potential function $\varphi(x, y, z)$ can be written as:

$$\chi(P) \equiv \theta(P)\varphi(P) + \int_{\Sigma} \left(\frac{\partial G(P,Q)}{\partial n}\varphi(Q) - G(P,Q)\frac{\partial \varphi(Q)}{\partial n}\right) dQ = 0 \quad (1)$$

Where G(P,Q) is the Green's function, and P and Q are called the source point and the field point, respectively with χ(P), the function that is characteristic of the open 3D domain. Physically, G(P,Q) represents the effect observed at a point P of a unit source at the point Q.

The term:

$$\frac{\partial G(P,Q)}{\partial n} \quad (2)$$

is the partial derivative of the function G with respect to the unit outward vector, which is normal at the point P or Q, on the boundary surface. This integral equation can be derived from the Laplace equation by applying Green's second theorem.

The power of the integral equation above, lies in the fact that it relates the potential φ and its derivative on the boundary alone, with no reference made to φ at points inside the domain. In a typical boundary-value problem, it may be given the following data:

$$\varphi(Q), \frac{\partial \varphi(Q)}{\partial n} \quad (3)$$

Or a combination of such data on the surface; Then, the integral equation above is a means of determining the unknown boundary function(s) from given boundary data.

To apply the BEM concepts to the problem of a sample of gypsum, having a flaw, and subjected to stress, consider a sample as the one shown in figure 13.

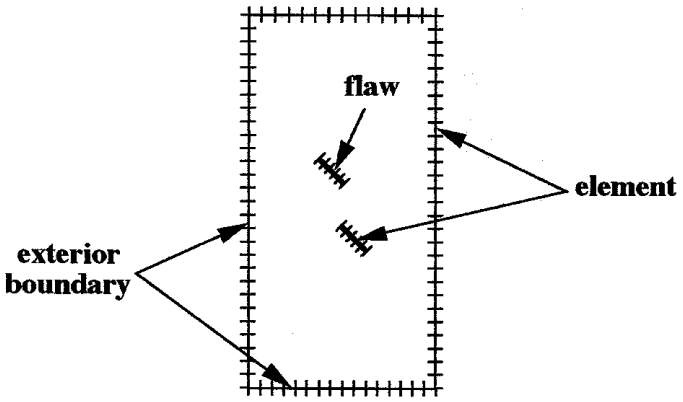

Figure 13: Discretization of specimen with boundary elements by Bobet & Einstein (1998a)

The internal and external boundaries of the sample can be discretized by 'N' numbers of different straight elements, which may have one or more reference points, having each reference point, two possible types of displacements: sliding and opening.

Figure 14(a) shows a reference point with two fundamental variables V_1 and V_2, representing sliding and opening displacements, respectively. Compressive stresses are positive (Figure 14 (b)).

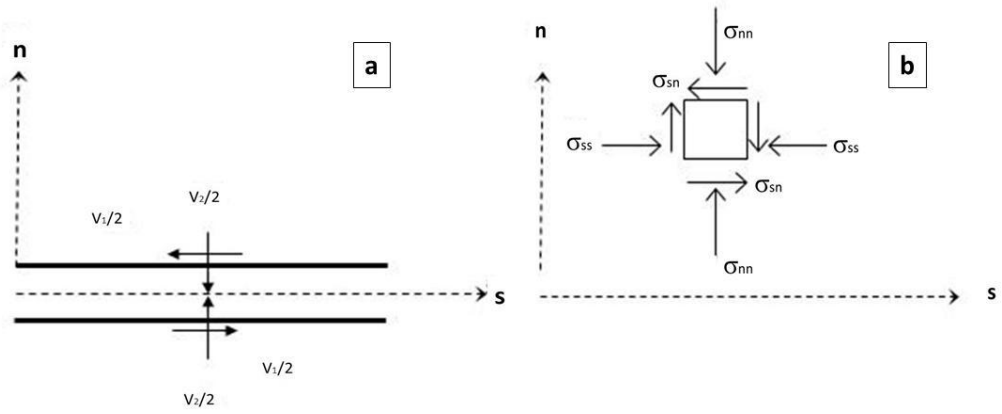

Figure 14: A displacement discontinuity element with stress conventions. (a) Fundamental variables, (b) stress convention (bobet & Einstein (1998b))

If the medium is discretized with *n* different elements, having each element one to *M* reference points, the stresses and displacements at the reference point *m* are given by:

$$\sigma_m = \{\sigma_{m,ss}, \sigma_{m,nn}, u_{m,ss}, u_{m,nn}\} \text{ for } m = 1 \text{ to } M \quad (4)$$

The stresses and displacements at any point in the body can be determined by linear superposition, as the contribution of all the elements in the medium, as elasticity is assumed in the model;

$$\sigma_{m,k} = A_{m,k,j} V_j \text{ (k= 1 to 4)} \quad (5)$$

In the equation above, V_j is the fundamental variable ranging from 1 to 2*M* (assuming two fundamental variables per reference point) and $A_{m,k,j}$ is the influence function of a unit change in the fundamental variable 'Vj' on the stress component 'k' of the reference point 'm'. The analytical solution that determines the stresses and displacements at any point in the medium due to a unit change in the variables is called the influence function of that variable. On the other hand, Eq. (4) can also be written in incremental form, as follows:

$$\sigma_{m,k}^{\Delta t} = A_{m,k,j} V_j^{\Delta t} \quad (6)$$

This equation represents a linear system of '*4M*' equations. Since displacement and stresses at each reference point in the boundary are known, a system of '*2M*' known equations will be produced. In addition, at each reference point, two fundamental variables, sliding and opening movements are unknown. Therefore, a system of '*2M*' equations with '2M' unknowns, obtained from Eq. (3), can be solved in order to find $V_j^{\Delta t}$. Once $V_j^{\Delta t}$ are found, the '2M' known equations will provide the rest of

undefined boundary conditions. Thereafter, the displacements and stresses at each point can be calculated, stating the system of equations based from integral equations expressions, base of the Boundary element method.

Considering the body having a domain surrounding by a boundary, the displacement boundary integral equation relating the boundary displacements, with the boundary stresses, can be written as:

$$\int t_i u_i^* dT + \int b_i u_i^* dT = \int u_i t_i^* dT + \int u_i b_i^* dT \quad (7)$$

3.1.2 Stress based crack initiation criterion

In the stress based criterion (Bobet, 1998b), the crack initiation depends on the local stress relative to the strength of the material, rather than the Stress Intensity Factors (SIFs), establishing a comparison between local stress states and the strengths of the material. From this comparison, if the calculated stress exceeds the strength of the material, the cracking process initiates.

As the stresses at the tip of a crack are much higher than the strength of the material, a plastic zone of radius r_0 is assumed to form at the tip of the crack, being identified as the fracture process zone in linear elastic fracture mechanics, Figure 15(a). The radius of the plastic zone, r_0, is assumed to be a material property, depending on the type of loading, being the size of the core different in uniaxial loading, biaxial loading, or in tension.

The first step is the calculations of the radial and tangential stresses at the boundary of the core region centered on the crack tip in order to compare the computed stresses with the material strength. This comparison can lead to two different conditions, according to Figure 15(b).

- Stresses are below the critical values - No propagation happens
- Stress exceeds the material strength and critical values - crack propagation happens.

Figure 15(c) shows the mathematical formulation of the propagation criterion. A tensile crack will initiate when the tangential tensile stress, $\sigma_\theta(r = r_0)$ reaches the critical tensile strength of the material σ_{crit} and the tensile crack initiates along the direction perpendicular to the direction of maximum tensile stress. Similarly, a shear crack initiates when the shear stress, $\tau(r = r_0)$ reachs the critical shear strength of the material, τ_{crit} and the shear crack initiates in the direction of the maximum shear stress. Figure 15(d) shows the corresponding failure envelope considered for this criterion. Therefore, three material parameters are needed for the analysis:

(a) Tensile strength of the material, σ_{Crit}

(b) Shear strength of the material τ_{crit}

(c) Radius of the plastic zone around the crack tip, r_0.

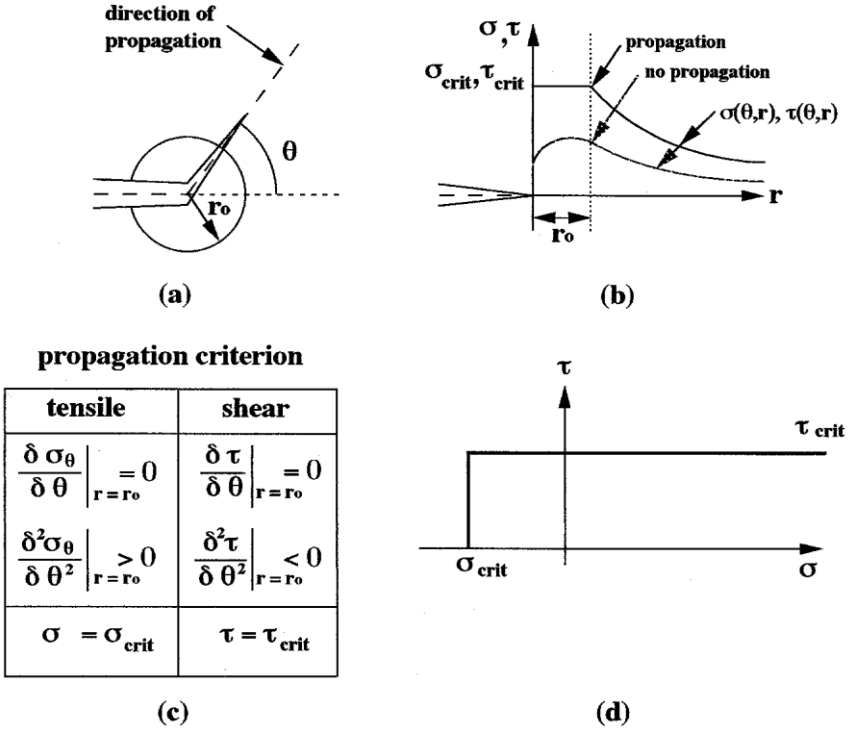

Figure 15: Crack initiation and propagation criterion. (a) plastic core region, (b) crack propagation criterion, (c) mathematical formulation, and (d) failure envelope (Bobet & Einstein, 1998b)

For uniaxial compression simulations, the core radius is taken as $r_0/a = 0.036$ (Bobet & Einstein, 1998b). These results are obtained by trial and error, by fitting the numerical predictions with experimental results. For the numerical predictions, $\tau_{crit} = -3.2$ MPa and $\sigma_{Crit} = 34.5$ MPa are assumed for gypsum (Bobet and Einstein, 1998b).

3.1.3 Model description and input parameters for FROCK

The scope of the current model is to predict the development of primary cracks previously observed experimentally, and recognized as tensile wing cracks. The material properties of molded gypsum are obtained from unconfined compression and tensile tests. These properties, to be used in the numerical modeling, are summarized in Table 1:

Table 1: Input Material properties for FROCK predictions (Bobet and Einstein (1998b))

Uniaxial compressive strength (MPa)	Tensile strength (MPa)	Young's Modulus (GPa)	Poisson's ratio
34.5	3.2	5.960	0.15

The material has a single flaw, assumed to be homogeneous, isotropic, and linear elastic. The flaw is oriented in 45˚ respect to the horizontal and its length is 2a=12.7 mm, considered to be close but free to open. A Friction coefficient of $\mu = 0.1$ is considered on both the flaw surface and the created cracks in the model. The ratio of $r_0/a = 0.036$ has been considered in defining the core radius around the crack tip (i.e., $r_0 = 0.2286$ mm).

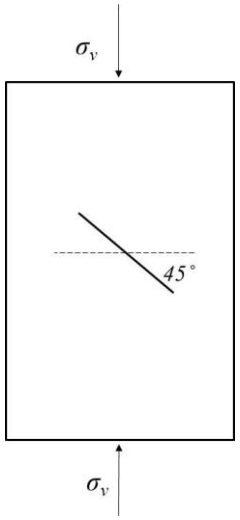

Figure 16: The model used in FROCK

The crack line has been discretized into 15 equal elements and constant stress σ_v has been applied in an infinite medium.

3.1.4 Results and discussion

The results obtained from the simulations in FROCK are shown in Figure 17. The wing crack initiation stress occurs at 2.11 MPa, being the tensile wing crack first initiated at the tip of the crack and as the load increased, propagated in a curvilinear path towards the boundaries of the specimen, along the direction of maximum compressive stress, as seen in the literature review.

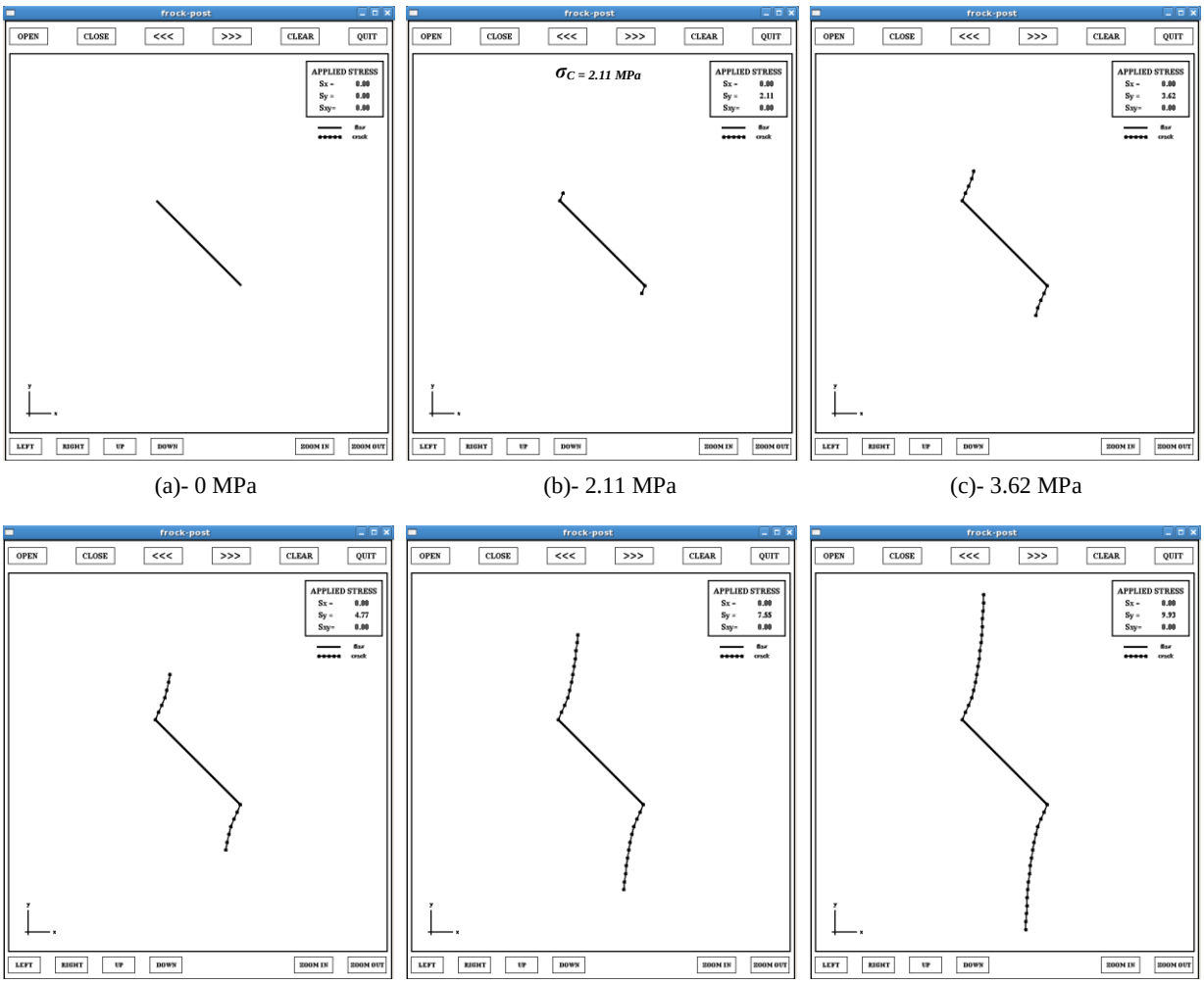

(a)- 0 MPa (b)- 2.11 MPa (c)- 3.62 MPa

(d)- 4.77 MPa (e)- 7.55 MPa (f)- 9.93 MPa

Figure 17: Modeling of crack initiation and propagation in molded gypsum containing a 45˚ single flaw in uniaxial compression

The predicted cracking behavior by FROCK is in good agreement with experimental observations presented in the literature review. To verify the values of the FROCK model, a comparison between a closed-form theoretical solution for stress intensity factors (SIFs), and those calculated by FROCK at the tip of the crack, is done.

Close form solutions of stress intensity factors in mixed mode loading, at the tip of the cracks, for any orientation, are provided in literature (Maugis, 1992). These equations, valid for open and closed cracks are as follows:

For the open flaws:

$$K_I = \frac{\sqrt{\pi a}}{2}[(1+k) + (1-k)cos\ 2\beta\ ]\ \sigma_V \quad (8)$$

$$K_{II} = \frac{-\sqrt{\pi a}}{2}(1-k)sin2\beta\ \sigma_V \quad (9)$$

For the closed flaws:

$$K_I = 0 \quad (10)$$

$$K_{II} = \frac{\sqrt{\pi a}}{2}[(1-k)sin2\beta - \mu[(1+k) + (1-k)cos2\beta\ ]\ \sigma_V \quad (11)$$

Being a, half of the flaw length, β the flaw inclination angle, k is the ratio of horizontal to vertical applied load, and μ is the friction coefficient for closed flaws. In this model, the flaw with 45˚ respect to the horizontal, Equations 4 to 7 can be reduced to:

For the open flaws:

$$\mathrm{K_I} = \frac{\sqrt{\pi a}}{2}\ \sigma_V\ ,\ \mathrm{K_{II}} = \frac{-\sqrt{\pi a}}{2}\sigma_V \quad (12)$$

For the closed flaw:

$$\mathrm{K_I} = 0\ ,\ \mathrm{K_{II}} = -\frac{\sqrt{\pi a}}{2}[1-\mu\ ]\ \sigma_V \quad (13)$$

In Table 2, the comparisons of obtained stress intensity factors at the flaw tips, obtained from FROCK and those from closed form solution.

Table 2: Comparison of obtained SIFs form FROCK with theoretical values

Stress Intensity Factors, $(MPa.\sqrt{mm})$	FROCK		Theory (Maugis, 1992)	
	K_I	K_{II}	K_I	K_{II}
Open flaw	2.2785	-2.2785	2.2332	-2.2332
Closed flaw	0	2.0503	0	2.0098

It should be remarked that the calculated SIFs in FROCK are almost identical to the theoretical values obtained here, confirming the accuracy of the modeling and validates the predicted cracking behavior.

3.2 Finite element methods

A brief introduction on cohesive zone and XFEM models will be presented in order to understand the basic principles of the tools used in the solution of the problem.

When considering failure, most engineering materials are not perfectly brittle as assumed by the Griffith theory, displaying some ductility after reaching the strength limit. There is a small zone right in the crack tip, in which there is small scale yielding, micro-cracking and void initiation takes place. If this fracture process zone is sufficiently small compared to the structural dimensions, linear-elastic fracture mechanics concepts apply. If this is not the case, the cohesive forces that exist in this fracture process zone must be considered, and cohesive-zone models must be used.

In cohesive-zone models, the degradation mechanisms in front of the crack tip are simplified to a discrete line or plane as the one in Figure 18, having a stress–displacement relationship across this line or plane, representing the degradation of the mechanisms in the fracture process zone.

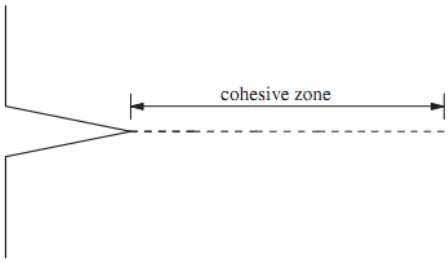

Figure 18: Schematic representation cohesive zone

Cohesive zone models consider that fracture is a gradual phenomenon in which separation of elements takes place across an extended crack 'tip', or cohesive zone, resisted by cohesive tractions. Cohesive elements do not represent any physical material, but describe the cohesive forces when material elements are separated, being placed between continuum elements, as shown in figure below:

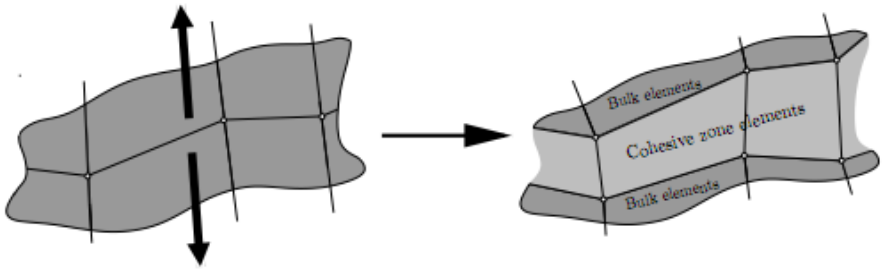

Figure 19: Application of cohesive zone elements along the bulk element boundaries

When a crack grows, these cohesive zone elements open in order to simulate crack initiation or crack growth. As the crack path only follows these elements, crack propagation strongly depends on the mesh of the cohesive zone elements.

In two dimensions, tractions can occur in the normal and the shear direction, and therefore, the failure description and its behavior is defined by traction-separation laws, which describes the tractions as a function of separation and determine the constitutive behavior of cohesive zone models.

To give a more theoretical support of this, consider a traction vector T, acting on a cohesive surface, which has associated an interfacial potential, with normal and tangential components, T_n and T_t, respectively:

$$\boldsymbol{T} = -\frac{\partial \varphi(\Delta)}{\partial(\Delta)} \tag{14}$$

With $\Delta = (\Delta_n, \Delta_t)$.

The potential can be written as:

$$\varphi(\Delta_n, \Delta_t) = \varphi_n + \varphi_n exp\left(-\frac{\Delta_n}{\delta_n}\right)\left\{\left[1 - r + \frac{\Delta_n}{\delta_n}\right]\frac{1-q}{r-1} - \left[q + \left(\frac{r-q}{r-1}\right)\frac{\Delta_n}{\delta_n}\right] exp\left(-\frac{{\Delta_t}^2}{{\delta_t}^2}\right)\right\} \tag{15}$$

Where δ_n and δ_t represent characteristic separations, in such a way that $T_n(\delta_n) = \sigma_{max}$ and $T_t(\delta_n/\sqrt{2}) = \tau_{max}$.

σ_{max} and τ_{max} represent the maximum values of the normal traction and the shear traction respectively. Furthermore, $q = \varphi_t/\varphi_n$ and $r = \Delta'_n/\delta_n$, where $r = \Delta'_n$ is the value of Δ_n when complete shear separation has taken place without resulting in normal tension $T_n = 0$. q will be taken equal to one and r equal to zero. The resulting equations for the normal and shear tractions are derived by combining the two equations above to obtain:

$$T_n = -\frac{\varphi_n}{\delta_n} exp\left(-\frac{\Delta_n}{\delta_n}\right)\left\{\frac{\Delta_n}{\delta_n} exp\left(-\frac{{\Delta_t}^2}{{\delta_t}^2}\right) + \frac{1-q}{r-1}\left[1 - exp\left(-\frac{{\Delta_t}^2}{{\delta_t}^2}\right)\right]\left[r - \frac{\Delta_n}{\delta_n}\right]\right\} \tag{16}$$

$$T_t = 2\left(-\frac{\varphi_n \Delta_t}{{\delta_t}^2}\right)\left\{q + \left(\frac{r-q}{r-1}\right)\frac{\Delta_n}{\delta_n}\right\} exp\left(-\frac{\Delta_n}{\delta_n}\right) exp\left(-\frac{{\Delta_t}^2}{{\delta_t}^2}\right) \quad (17)$$

φ_n and $\varphi_t$are the areas under the normal traction separation curve and the shear traction curve respectively. They represent the amount of work needed to complete separation. This can be seen for q=1, r=0, and assuming that $T_n = T_n(\Delta_n, \Delta_t = 0), T_t = T_t(\Delta_n = 0, \Delta_t)$, for which case, the so called uncoupled tractions are obtained. Using $T_t(\delta_n) = \sigma_{max}$ and $T_t(\delta_n/\sqrt{2}) = \tau_{max}$ the following relations for φ_n and $\varphi_t$can be obtained:

$$\varphi_n = \sigma_{max} \exp(1)\delta_n \ ; \varphi_t = \sqrt{\exp(1)/2}\, \tau_{max}\delta_n \quad (18)$$

The normalized traction curves for uncoupled normal separation and shear separation are shown in Figure 20. The values T_n/σ_{max} and T_t/τ_{max} represent the dimensionless normal and shear tractions. Δ_n/δ_n and Δ_t/δ_t represent the dimensionless normal and shear openings. The normal traction-separation curve shows that starting from an opening of zero and increasing the separation also increases the traction until a maximum value is reached at δ_n. After the cohesive force decreases until the cohesive zone no longer has any stiffness in normal direction. When the cohesive zone is given a separation displacement in negative direction, the traction rapidly becomes more negative in order to prevent penetration. The shear traction separation curve does not show such a behavior for negative separations. Separations in negative direction merely lead to shear tractions in the negative directions, which are opposite to those for a positive Δ_t. Even this introduction to cohesive zone model was done for a 2D case, it can be extended to three dimensions by adding a new tangential traction to the set of equations, directing perpendicular to the other two already studied.

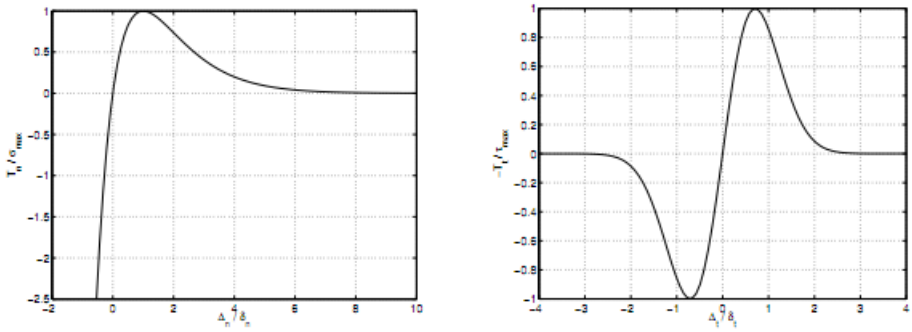

Figure 20: Left – Normal traction curve for the uncoupled modeling; right – Shear traction curve for the uncoupled modeling

3.2.1 Model description and input parameters for the cohesive zone model

The commercial software ABAQUS(c) is used to model the same geometry and properties of the gypsum specimen described in section 3.1.4, except for the crack tip; in the cohesive model the crack was assumed to be sharp. In addition, additional parameters that are required for the cohesive model were calibrated based on the crack initiation stress; we specified the displacement at failure at 10^{-3}mm with exponential decay. In addition, we assumed the ration between the stiffness of the cohesive zone to the elastic modulus to be the same in all direction and we assigned that ratio to 10^8. The traction separation curve is shown in the following Figure.

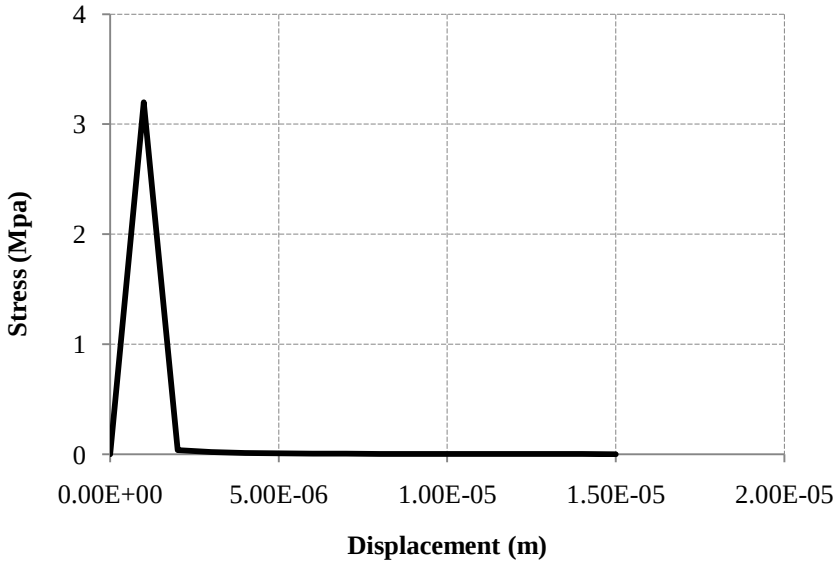

Figure 21: Stress-displacement curves used in the cohesive model

The model is divided into two regions; the first region is elastic with CPE4RH elements (A 4-node bilinear plane strain quadrilateral). The second region is where the initial crack was specified and the cohesive elements were inserted (COH2D4 elements A 4-node two-dimensional cohesive element), as shown in the following Figure.

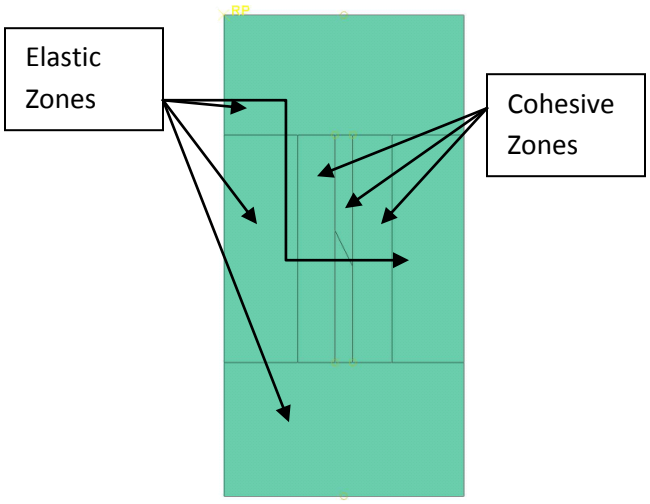

Figure 22: Section Assignments in the cohesive model

In the cohesive zone model, the crack propagation is highly dependent on the model discretization. ABAQUS[(c)] has limited options on the type of elements where the cohesive zones could be used, as such we only used what is available without writing a subroutine for different element shape. Ideally, a triangular element will be suitable for such application, however, only linear quadrilateral elements could be used. The other factor that play a major role in the prediction of the crack propagation is the mesh size, as we are using a quasi static loading, the required element size is a function of the length of fracture process zone, which was estimated based on Bobet and Einstein (1998b) to be on the order of 0.6mm. We performed two analysis; one with approximately two element per length of fracture process zone and the other with two elements per crack length (mesh dimension is approximately 6 mm). The coarse and fine meshes are shown in Figure 23.

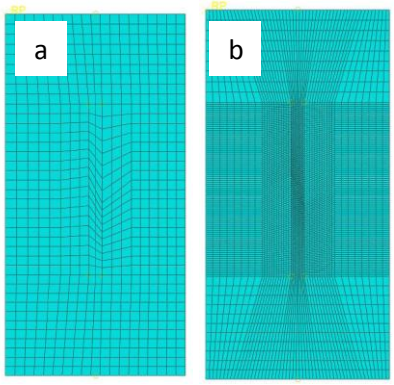

Figure 23: Model Discretization a- Coarse Mesh, b- Fine Mesh

For the boundary conditions, we assigned rollers at the four corners to restrict the movement in the 1-direction. The loading scheme was a displacement control loading with a uniform displacement at the top and bottom boundaries of 1mm quasi static loading.

3.2.2 Analysis results and discussion for cohesive zone model

The results are as anticipated from the cohesive mode, the crack propagates along the elements boundary, when the failure displacement is reached. The deformed shape for both the coarse and fine meshes are shown in figure 24:

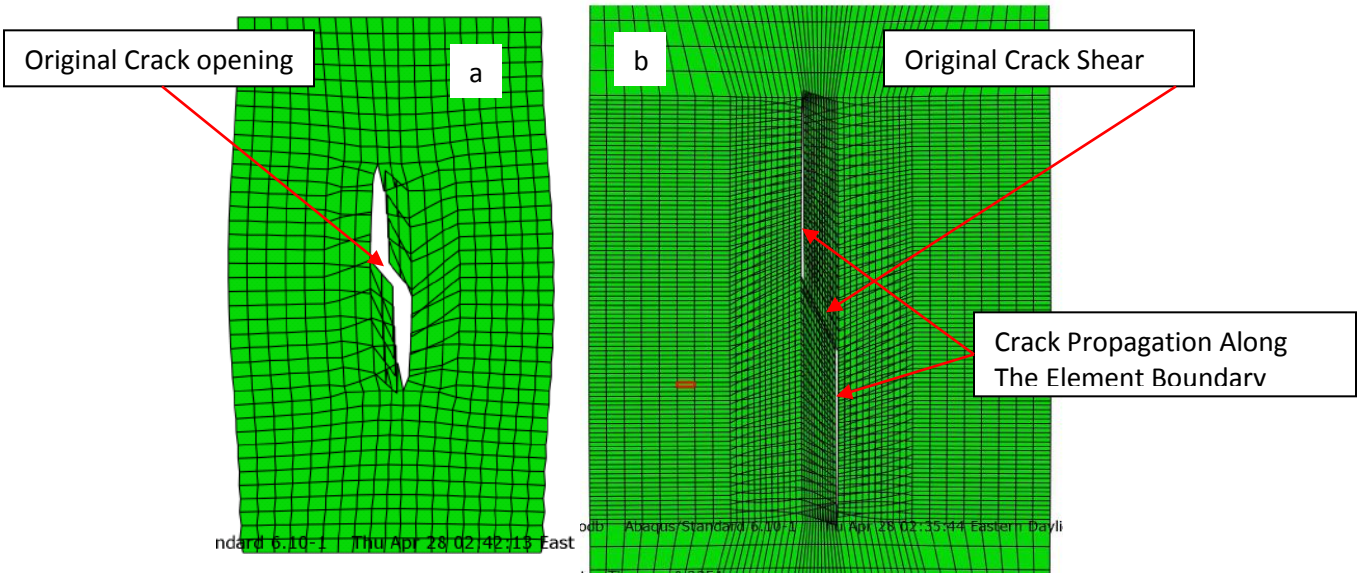

Figure 24: Deformed Mesh (X8) a- Coarse Mesh, b- Fine Mesh

Based on the experimental studies summary from the previous sections (See Figure 10), it appears that the original crack opening in the coarse mesh is unrealistic. A more realistic prediction is observed from the fine mesh model. However, for both mesh sizes, the wing crack propagated vertically and this is due to the limitation of the cohesive model.

The crack propagation at various stress levels is shown in the following figure, it should be noted that the stresses are the ones at the cohesive zone boundary.

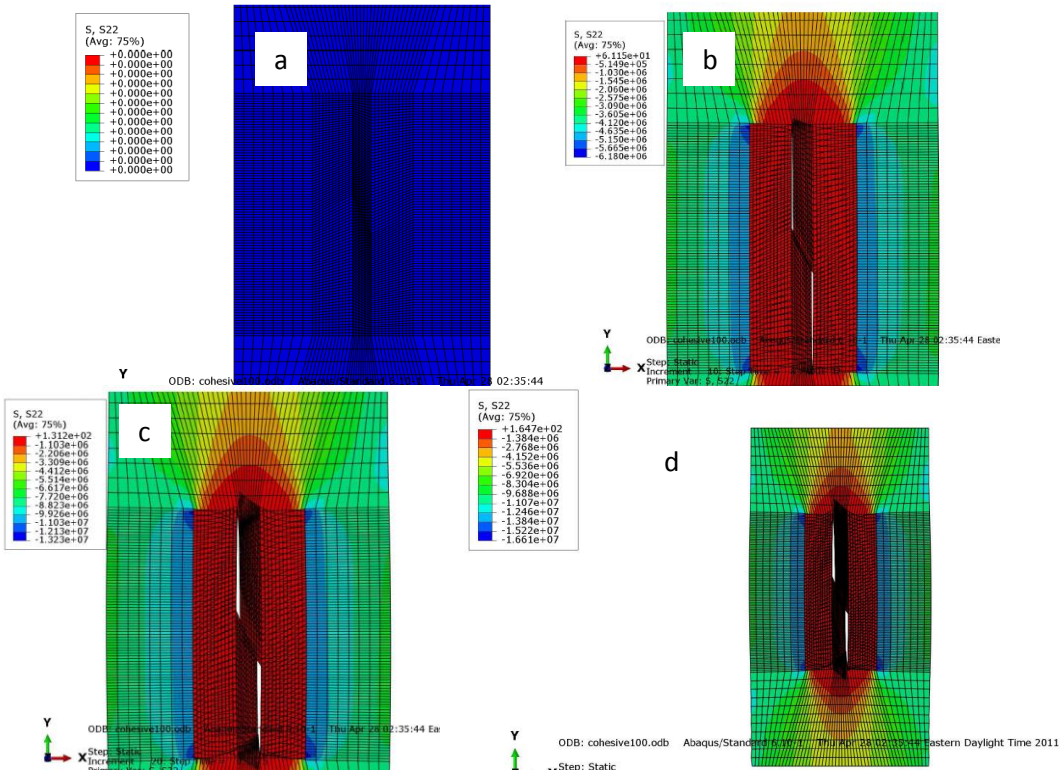

Figure 25: Crack Propagation (X20) a- 0 MPa, b- 5.15 MPa, c- 11.0 MPa and d- 13.8 MPa

It can be observed from Figure 25 that the S22 stress is uniform in the cohesive zone region once the crack starts propagating, this is a limitation of the cohesive zone model, when the crack is propagating in a different direction than the crack plane.

From the above discussion, it can be concluded that the cohesive zone model is more appropriate for a crack propagation in the direction of the crack plane. Triangular elements with better defined parameters may result in a better prediction.

3.2.3 The Extended Finite Element Method (XFEM)

The extended finite element method (XFEM) is a numerical technique that extends the classical finite element method (FEM) approach by enriching the solution space for solutions to differential equations with discontinuous functions. It is a useful approximation for solutions with pronounced non-smooth characteristics in small parts of the computational domain that is being analyzed, as discontinuities and singularities, enabling optimal convergence rates for these applications. In this case, a single mesh suffices for modeling as well as capturing the evolution of material interfaces and cracks in two- and three-dimensions.

The basic philosophy of the X-FEM is that features of interest in a problem, for example crack surfaces, phase boundaries, and fluid-structure interfaces, can be represented independently of the finite element mesh. As a result, simulating the evolution of these features is greatly facilitated. This is particularly true for crack analysis and branching, with no need to explicitly "fit" these features, avoiding re-meshing in many cases and facilitating adaptivity in others. With the X-FEM, the classical mesh needs only overlap the geometry of the crack front and does not need to be aligned with it. The linear combination is then augmented with enrichment functions that capture the jump in displacement field across the crack, being possible to simulate this through the identification of additional enriched nodes and a new construction for the enrichment function, a process much simpler than re-meshing.

Most finite element approximations to bulk fields (e.g. displacement, temperature) can be expressed as a linear combination of nodal shape functions. These shape functions are only able to represent discontinuities in the bulk fields if the mesh is constructed in a particular way.

In the XFEM method, special functions describing the field behavior of a body are incorporated locally into the finite element approximation space, and the resulting space is capable of capturing all the features of interest, independently of the geometry, and without the need to remesh the discretization of the body.

A one dimensional model will be used as an example to show the XFEM methodology, and explain how it locally enriches the field to capture the desired features of interest in the solution.

The XFEM uses the same basic ideas of standard FEM, discretizing a domain into sub domains, $\aleph = \{\aleph_1, \aleph_2, \aleph_3 \dots \aleph_N\}$, having the nodes at the vertices of the elements, coordinates denoted by $x = \{x, x_2, x_3 \dots x_N\}$. With this, each node can have an interpolation function associated, $\emptyset_i$. Then, the standard FEM interpolation will be given by the approximation:

$$u = \sum_{i=1}^{i=N} \emptyset_i (X) u_i \tag{19}$$

In order to approximate the field correctly, it is needed a search for a function that can capture local features of interest. Assuming the existence of a discontinuity, let g(X) be the local approximating function that can approximate the field U in the region of the given discontinuity. The function g(X) could take a form of a Heaviside H(X) function, as it represents a jump and can describe properly discontinuities.

Now, it is possible to define a region D with domain $\square_{PoU}$ in the interval $\{x_i, x_{i+1}\}$, where we want the enrichment of the field, i.e, element is required to be enriched with the function g(X) = H(X).

In order to incorporate the local enrichment into the Finite element approximation, the nodes of the element $\square_3$ is enriched with enrichment function g(X). Then the next step is to find functions which sums up to unity in the region D. From finite element theory, it is known there are shape functions satisfying this condition, and then it is possible to use the same interpolation functions, i.e $\emptyset_3$ and $\emptyset_4$ functions partitioning the unity, hence:

$$\sum_{i=1}^{i=N} \emptyset_i = 1 \tag{20}$$

It should be noted that other different functions could also be used to sum up a unity function, but in this case, the most convenient are used for the purpose of the analysis. Now using the notion of partition of unity the enrichment function g(X) can be included as:

$$\sum_{j=i-1}^{j=i} \emptyset_j g(X) a_j = 1 \tag{21}$$

Where the terms a_j are unknown enriched degrees of freedom. With this, the extended approximation of FEM can now be expressed as:

$$u = \sum_{i=1}^{i=N} \emptyset_i u_i + \sum_{j=i-1}^{j=i} \emptyset_j g(X) a_j \tag{22}$$

Where the first summation is for the entire space of nodes, while the second summation considers the enriched nodes, which are a subgroup of the entire space of nodes. It is worth saying that only a region near the discontinuities such as cracks, holes, material interfaces is enriched with enrichment functions.

3.2.4 Model description and input parameters for the XFEM model

We utilized the commercial software ABAQUS[(c)] to model the same geometry and properties of the gypsum specimen described in section 3.2.1. We assigned one material for the model with elastic properties and a damage criterion (MAXPS) with the same properties as the Cohesive Zone Model. We specified the crack enrichment zone to allow for crack propagation, as shown in the following figure. We used the CPE4RH elements (A 4-node bilinear plane strain quadrilateral).

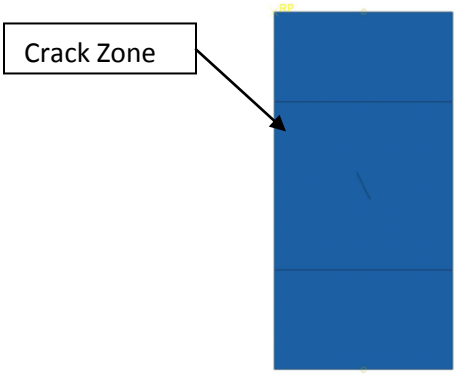

Figure 26: Crack Enrichment Zone in the XFEM model

To identify the suitable mesh size we ran few models with different mesh coarseness. The following figure shows the mesh for two cases one with approximately two element per length of fracture process zone and the other with four elements per crack length (mesh dimension is approximately 3 mm). The coarse and fine meshes are shown in the following Figure.

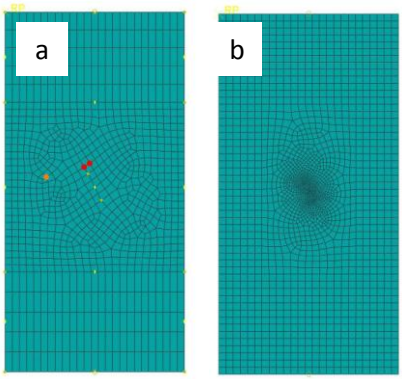

Figure 27: Model discretization a- Coarse Mesh, b- Fine Mesh

For the boundary conditions, we assigned rollers at the four corners to restrict the movement in the 1-direction. The loading scheme was a displacement control loading with a uniform displacement at the top and bottom boundaries of 1mm quasi static loading.

3.2.2.1. Analysis results and discussion for the XFEM model

The results are as anticipated from the cohesive mode, the crack propagates along the elements boundary, when the failure displacement is reached. The deformed shape for both the coarse and fine meshes are shown in the following Figure.

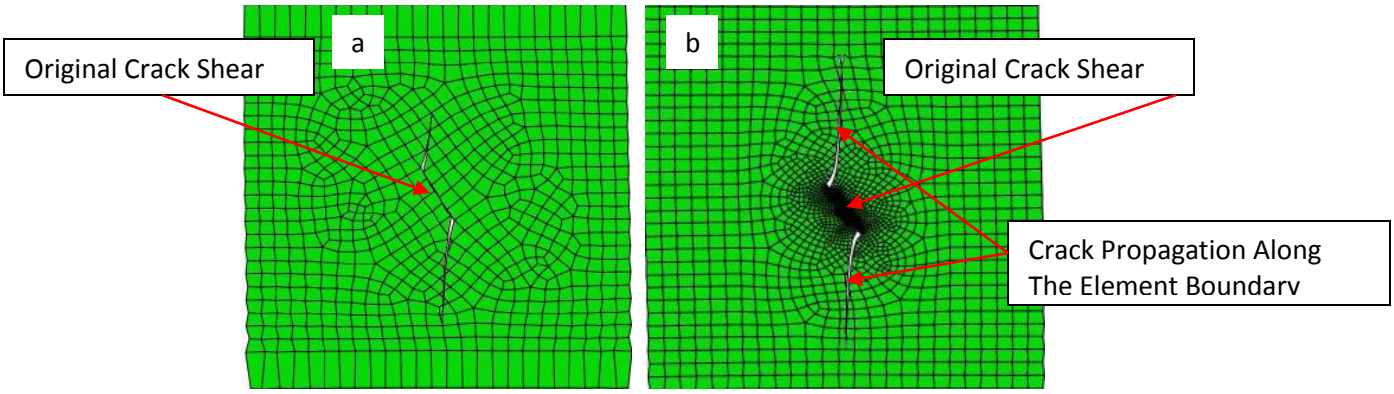

Figure 28: Deformed Mesh (X10) a- Coarse Mesh, b- Fine Mesh

Based on the experimental studies summary from the previous sections (See Figure 10), it appears that the original crack opening in both mesh configurations is realistic. However, the fine mesh captured the wing cracks on both sides more accurately. The wing cracks propagated as was observed in the experimental studies, the fine mesh sowed more curvature towards the boundaries, which is an accurate capturing of the behavior from the experimental study summarized in the previous sections.

The crack propagation at various stress levels is shown in the following figure, the stress are the far field stresses at the boundary in the 22-direction (Vertical Stress)

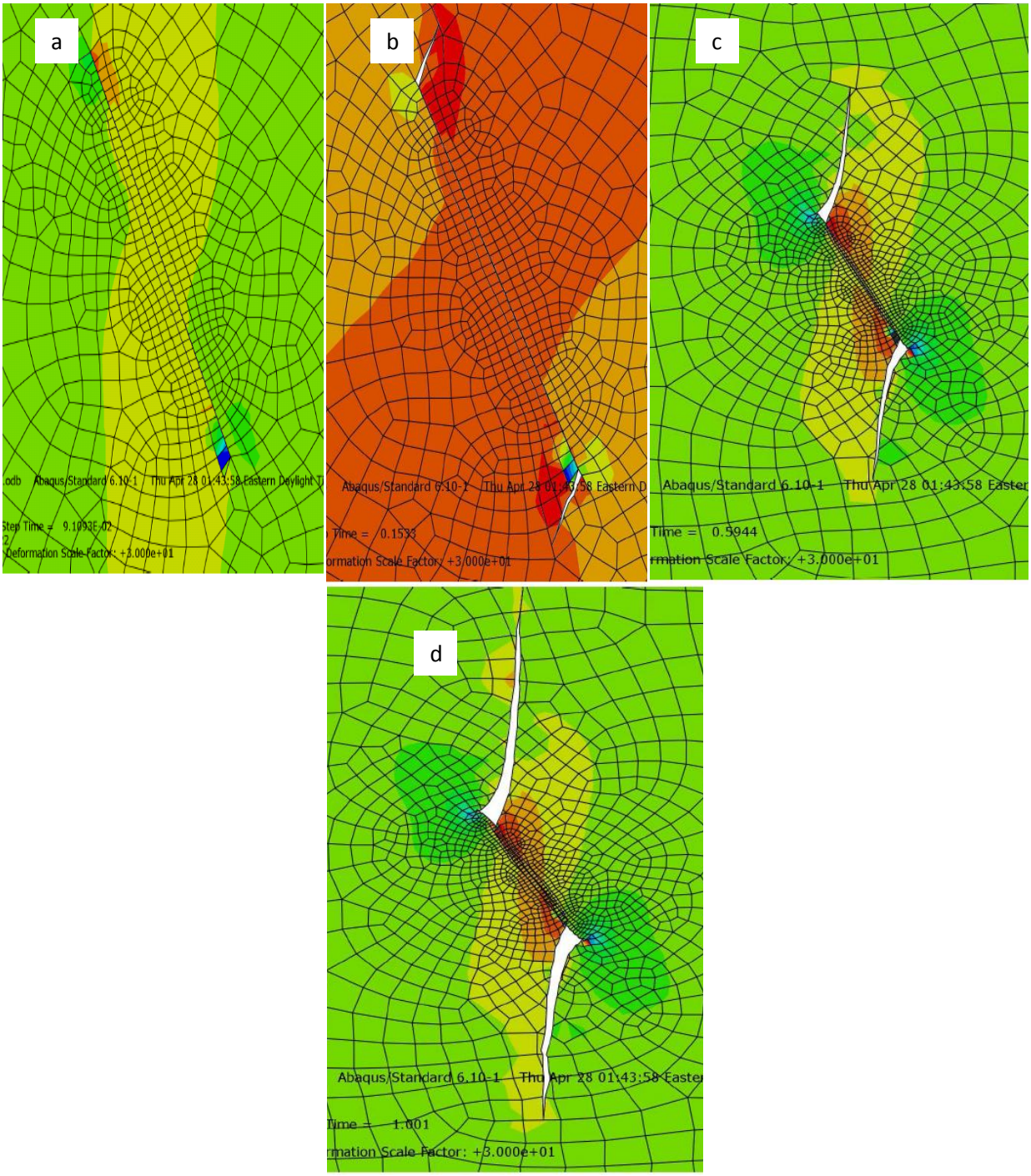

Figure 29: Crack Propagation (X20) a- 4MPa, b- 8.5MPa, c- 18MPa, and d-65MPa

It can be observed from the above figure that the S22 changes around the crack tip are captured. In figure 28a, is the offset of crack propagation, which is approximately twice of what was observed in the BEM. It is obvious that the crack propagation path follows the maximum tensile stress. In addition, a

secondary shear crack is formed at the crack tip at higher stress (figure d), which is good agreement with the published experimental data.

In addition, we estimated the stress intensity factor for the mixed mode from the analysis result to be between 1.9 and 2.2 at the offset of crack propagation, which is in good agreement with the results from the boundary element method and the theoretical estimates presented in table 2.

The energy used to create new surfaces shows the brittle nature of the material, as sudden jumps in the used energy. The following graph shows the energy used in creating new surfaces (crack propagation).

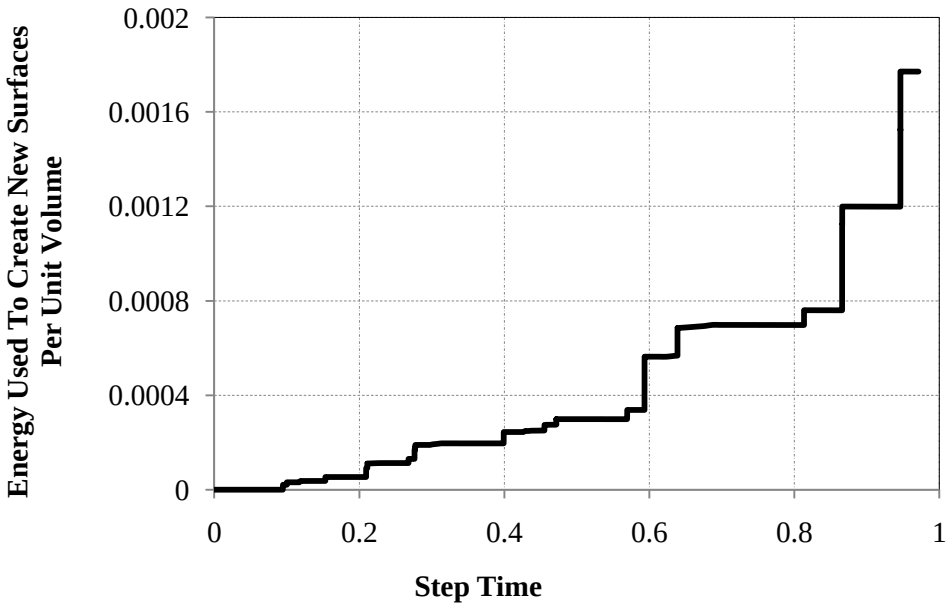

Figure 30: Energy Used To Create New Surfaces

It appears that the XFEM performed well in predicting the crack propagation in brittle material. The model showed good agreement with the published experimental results and the boundary element method.

4 Conclusions

It can be concluded that the numerical simulation of crack propagation in general requires great attention to details of the model, such as the mesh size, element type, and modeling technique and most important the selected constitutive model for traction separation and its properties.

The boundary element method showed a very good agreement with the published experimental data and the ABAQUS predictions.

The cohesive element method showed good prediction of the wing crack propagation within the limitation of the method. However, it did not predict the stresses around the crack tip. The crack followed the element boundary. A triangular element will result in a better prediction using the cohesive model. In addition, the accurate prediction of the crack initiation and propagation direction depends is very sensitive to the estimated value of the cohesive surface stiffness in various directions.

The extended finite element model (XFEM) showed good agreement with the published experimental data in predicting the shape of the wing crack. Also, it showed ability for a reasonable estimate of the stress at the crack propagation offset. In addition, the stress intensity factor for a mixed mode was estimated accurately from the XFEM model. The selection of the damage criteria should be determined carefully based on the available parameters. It is highly recommended that the model parameters are calibrated against experimental data before commencing any detailed analysis.

The variations between the BEM and the XFEM were limited and they are due to different constitutive relations used in each of the models.

5 References

[1]. Bobet, A. and Einstein, H.H. (1998a): Fracture coalescence in rock-type materials under uniaxial and biaxial compression. Int J Rock Mech, Min Sci 35 7, pp. 863–888.

[2]. Bobet, A. and Einstein, H. H. (1998b): Numerical modeling of fracture coalescence in rock materials. Int. J. Fracture 92, 221-252.

[3]. Bobet, A. (1997): Fracture coalescence in rock materials: experimental observations and numerical predictions. Sc.D. Thesis, MIT, Cambridge, U.S.A.

[4]. Chan, H.C. (1986): Automatic two-dimensional multi fracture propagation modeling of brittle solids with particular application to rock. Sc.D. Thesis, MIT, Cambridge, U.S.A.

[5]. Chen, G., Kemeny, J.M. and Harpalani, S. (1995): Fracture propagation and coalescence in marble plates with pre-cut notches under compression, Symp fractured jointed rock masses, Lake Tahoe, CA, pp. 435–439.

[6]. Chan, H. C. M., Li, V. and Einstein, H. H. (1990): A hybridized displacement discontinuity and indirect boundary element method to model fracture propagation. Int. J. Fracture 45,263-282.

[7]. Huang, J.F., Chen, G.L, Zhao, Y.H. and Wang, R. (1990): An experimental study of the strain field development prior to failure of a marble plate under compression, Tectonophysics 175, pp. 283–290.

[8]. Ingraffea, A.R. and Heuze, F.E. (1980): Finite element models for rock fracture mechanics, Int J Num Anal Meth Geomech 4, p. 25.

[9]. Lajtai, E.Z. (1974): Brittle fracture in compression, Int. J. Fracture 10, pp. 525–536.

[10]. Li, Y.P., Chen, L.Z., and Wang, Y.H. (2005): Experimental research on pre-cracked marble under compression, Int J Solids Struct 42, pp. 2505–2516.

[11]. Maugis, D. (1992): Stresses and displacements around cracks and elliptical cavities: exact solutions. Engineering Fracture Mechanics 43(2), 217–255.

[12]. Petit, J. and Barquins, M. (1988): Can natural faults propagate under mode II conditions?, Tectonics 7 (6), pp. 1246–1265.

[13]. Wong, N.L.Y. and Einstein, H.H. (2009): Systematic evaluation of cracking behavior in specimens containing single flaws under uniaxial compression. Int J Rock Mech, Min Sci 46 2, pp. 239–249.